



Published in final edited form as:

IEEE Trans Med Imaging. 2013 September ; 32(9): 1685–1697. doi:10.1109/TMI.2013.2263388.

Optimal Co-segmentation of Tumor in PET-CT Images with Context Information

Qi Song,

Biomedical Image Analysis Lab, GE Global Research Center, Niskayuna, NY 12309, USA. The work was mainly finished when he was with the Department of Electrical & Computer Engineering, The University of Iowa, Iowa City, IA 52242, USA

Junjie Bai,

Department of Electrical & Computer Engineering, The University of Iowa, Iowa City, IA 52242, USA

Dongfeng Han,

Department of Electrical & Computer Engineering, The University of Iowa, Iowa City, IA 52242, USA

Sudershan Bhatia,

Department of Radiation Oncology, The University of Iowa, Iowa City, IA 52242, USA

Wenqing Sun,

Department of Radiation Oncology, The University of Iowa, Iowa City, IA 52242, USA

William Rockey,

Department of Radiation Oncology, The University of Iowa, Iowa City, IA 52242, USA

John E. Bayouth,

Department of Radiation Oncology, The University of Iowa, Iowa City, IA 52242, USA

John M. Buatti, and

Department of Radiation Oncology, The University of Iowa, Iowa City, IA 52242, USA

Xiaodong Wu [Senior Member, IEEE]

Department of Electrical & Computer Engineering and the Department of Radiation Oncology, The University of Iowa, Iowa City, IA 52242, USA

Qi Song: song@ge.com; Junjie Bai: junjie-bai@uiowa.edu; Dongfeng Han: dongfeng-han@uiowa.edu; Sudershan Bhatia: sudershan-bhatia@uiowa.edu; Wenqing Sun: wenqing-sun@uiowa.edu; William Rockey: william-rokey@uiowa.edu; John E. Bayouth: john-bayouth@uiowa.edu; John M. Buatti: john-buatti@uiowa.edu; Xiaodong Wu: xiaodong-wu@uiowa.edu

Abstract

PET-CT images have been widely used in clinical practice for radiotherapy treatment planning of the radiotherapy. Many existing segmentation approaches only work for a single imaging modality, which suffer from the low spatial resolution in PET or low contrast in CT. In this work we propose a novel method for the co-segmentation of the tumor in both PET and CT images, which makes use of advantages from each modality: the functionality information from PET and the anatomical structure information from CT. The approach formulates the segmentation problem as a minimization problem of a Markov Random Field (MRF) model, which encodes the information from both modalities. The optimization is solved using a graph-cut based method.

Correspondence to: Xiaodong Wu, xiaodong-wu@uiowa.edu.

The first and second authors had equal contributions to this work.

Two sub-graphs are constructed for the segmentation of the PET and the CT images, respectively. To achieve consistent results in two modalities, an adaptive context cost is enforced by adding context arcs between the two subgraphs. An optimal solution can be obtained by solving a single maximum flow problem, which leads to simultaneous segmentation of the tumor volumes in both modalities. The proposed algorithm was validated in robust delineation of lung tumors on 23 PET-CT datasets and two head-and-neck cancer subjects. Both qualitative and quantitative results show significant improvement compared to the graph cut methods solely using PET or CT.

Index Terms

PET-CT; image segmentation; global optimization; graph cut; context information; lung tumor

I. Introduction

Accurate target delineation plays an increasingly important role in image-guided radiation therapy due to the high dose gradients achievable with the technology. Inaccurate delineation of target volumes by a small amount can result in either overdose of the surrounding tissues, dangerous underdose of the tumor, or both [1], [2]. For effective assessment of target volumes in cancer treatment, medical imaging modalities like Computed Tomography (CT) and Positron Emission Tomography (PET) are widely used. CT images usually have high resolution and provide detailed anatomical information. However, limited physiological information can be captured by CT imaging. Fig. 1(a) shows one typical example. Studies show that a large inter-observer variability has been observed for many tumor sites because the tumors usually have a very similar intensity distribution with surrounding soft tissues [3], [4] in CT images. To improve the visualization of tumor tissues, Positron Emission Tomography (PET) imaging with the metabolic tracer ^{18}F -FDG (Fluoro Deoxy Glucose) was introduced. In PET, target tumors generally have high standardized uptake values (SUVs), which helps to distinguish normal tissues from malignant tumors. However, due to the physically limited spatial resolution of PET and the method of visualization, the boundary of a lesion in PET can appear fuzzy and indistinct (see Fig. 1(b)). Thus accurate segmentation of tumors using only PET is still problematic. A number of studies have demonstrated that combining PET and CT information results in more consistent delineation of the tumor volumes [5], [6], [7], [8], [9]. The integrated PET-CT has recently become a standard method of imaging for radiation therapy treatment planning and has been increasingly used for tumor delineation.

Though PET-CT images have been routinely used in clinic, target delineation is still typically performed manually by the oncologist on a slice-by-slice basis with very limited support of automated segmentation tools. Many existing automated segmentation algorithms only work for single modality. Automated segmentation from co-registered PET-CT images remains challenging. In this work, we propose a novel method for co-segmentation of tumor in PET and CT images, which makes use of the advantages from both modalities: the superior contrast of PET and the superior anatomical resolution of CT. Our method strives to compute simultaneously, the tumor volume defined on CT as well as that defined on PET, which are not necessarily identical. The rationale is that PET and CT convey different information, which is not always complementary, but sometimes contradictory; so the tumor volumes defined on PET and on CT could be different. Our method is based on Boykov's graph cut method [10]. The basic idea of the graph cut method is to formulate the segmentation problem as an energy minimization problem. The energy encodes both boundary and region information, which can be minimized in the discrete space using the graph-based method. In this paper, we propose a novel energy representation, which incorporates the region and boundary information from both PET and CT images. To

achieve consistent segmentation results between two modalities, a novel context term is introduced into the energy function. The co-segmentation of PET and CT images is achieved by solving a *single* maximum flow problem, which leads to a globally optimal solution in low-order polynomial time.

The rest of the paper is organized as follows. In Section II, we give a brief review of the related work on tumor segmentation using PET-CT images, as well as the graph-based segmentation methods. In Section III, we introduce the proposed graph model, including the formulation of the energy and the corresponding graph construction. Section IV gives the detailed description of the lung tumor segmentation using the proposed graph model. Section VII discusses the novelty of the approach as well as its limitations. Finally, Section VIII draws the conclusion.

II. Related Work

A. Tumor Segmentation on PET-CT images

The usage of both PET and CT images for accurate target delineation in radiotherapy has attracted considerable attention in recent years. The most widely used PET segmentation method in clinical practice is thresholding based on SUVs, such as using an absolute SUV value [11], [12], a percentage of the maximum SUV [13], [14], [15], [16], [17] and many other variants [18], [19], [20], [21]. Among the thresholding methods, the signal-to-background ratio (SBR) algorithms are most commonly used [22], [18], [23], in which the threshold value is calculated depending on mean background accumulation and the signal of the lesion. Such a method requires an estimate of the lesion volume of interest before segmentation, which may not be easy at all. Recently, many more segmentation algorithms are brought in PET oncology from the field of Computer Vision [24]. Some of these approaches have been well known for other medical image modalities including the use of image gradients [25], [26], deformable contour models [27], [28], [29], mutual information in hybrid [30], [31], [32], [33], [34] and histogram mixture models for heterogeneous regions [35], [36], [37], [38]. However, almost all these methods can segment tumor either only on PET images or on the fused PET-CT images [29], [30], [39]. Wojak *et al.* developed a joint variational segmentation method which incorporates the PET information into the fuzzy segmentation model [40]. The method only computes a contour in CT, which is driven by the PET information. No precise segmentation is performed on PET data. Gribben *et al.* considered PET and CT as vectorial components with a covariance matrix linking two modalities, and solved the resulting MAP estimation problem using the Iterated Conditional Modes (ICM) algorithm [31]. The proposed approach aims to compute an identical tumor contour for PET-CT images. This may compromise the segmentation quality since PET and CT may convey different information, resulting a disagreement of the tumor volume defined on PET from that on CT.

The most closely related work is Han *et al.* [39]. In both our method and Han *et al.*'s, the PET/CT segmentation is formulated as an MRF optimization problem and is solved by computing a single maximum flow in the constructed graph. The key novelty of our method is the recognition of possible differences of tumor volume defined in PET from that defined in CT, which result in the delineation of true tumor boundaries in both modalities, rather than a compromised identical one. The introduction of the context term in the energy function provides a mechanism penalizing the contour difference in PET and CT while enabling the contour to follow the salient features in each modality to obtain a difference contour. To the best of our knowledge, no previous method is able to simultaneously delineate the tumor contours from PET and CT while allowing such differences. In Han *et al.*'s method, if PET and CT convey contradictory information, an arbitration term in the energy function is used to produce a compromised contour for both PET and CT, that is,

their method strives to compute a *single* compromised tumor volume from PET and CT. Thus, their method is also more sensitive to registration errors. To implement the arbitration mechanism, the size of the graph constructed from the input PET/CT images in Han *et al.*'s method is about three times the CT image size; while in our method, the graph size is just about two times the CT image size.

B. Graph-based Segmentation

Graph-based methods have been widely used for image segmentation. The main idea is to formulate the segmentation problem as a discrete energy minimization problem. Image features are incorporated by designing proper cost functions for energy terms. Felzenswalb *et al.* [41] used pairwise region comparison for image segmentation based on minimum spanning tree (MST) algorithm. Grady *et al.* [42] showed how to extend the shortest method for 3-D surface segmentation. Xu *et al.* [43] proposed a novel approach using shortest-path algorithm for multiple surfaces segmentation in 3-D. Wu and Chen [44] developed an optimal surface detection method based on maximum flow. Li *et al.* [45] extended the work for multiple interacting surfaces segmentation. A generalized version of the framework dubbed LOGISMOS was reported in [46], which allows simultaneous segmentation of multiple objects and surfaces. Most recently, Song *et al.* [47]'s method incorporates both shape and context prior knowledge for multiple surface segmentation.

Our work is inspired by the multiple surface detection method [45], [47] and the multi-region segmentation method [48] based on the graph theoretical framework. A separate appearance model is employed for each spatially distinct region in an image. Geometric interactions are incorporated between region boundaries. In our work, we extend the idea for co-segmenting objects in *multiple* images with different modalities. The tumor volumes defined on PET and on CT are viewed as two mutually interacting regions, which are segmented simultaneously. An adaptive context term is employed to encourage consistent segmentation in PET and CT.

III. Graph Model

The main idea of the proposed method is to formulate the segmentation problem as an energy minimization problem in the discrete space, which can be solved using a graph-based method. Two subgraphs are constructed, one for PET and one for CT. The weight of arcs in the subgraph encodes the boundary and region information from the corresponding image. The key point is the incorporation of context information between the PET and CT images, which is enforced by adding inter-subgraph arcs between correspondent nodes of two subgraphs. The node correspondence between the two subgraphs (i.e., the voxel correspondence between the PET and the CT images) can be established, for example, using image registration if necessary. It can be either one-to-one or multiple-to-one correspondence, in which one PET voxel may correspond to a set of CT voxels.

A. Energy Function

Consider a PET-CT image pair $(\mathcal{I}, \mathcal{I}')$, where \mathcal{I} denotes an input CT image and \mathcal{I}' denotes the registered PET image. For each voxel $v \in \mathcal{I}$, we have a correspondent voxel $v' \in \mathcal{I}'$. Let l_v and $l_{v'}$ denote the binary labels assigned to each voxel $v \in \mathcal{I}$ and $v' \in \mathcal{I}'$, respectively. In our notation, $l_v = 1$ ($l_{v'} = 1$) means that the voxel v (v') belongs to the target object. If $l_v = 0$ ($l_{v'} = 0$), then the voxel v (v') is considered to be in the background. The set of voxels whose label are 1 in \mathcal{I} (resp., \mathcal{I}') defines the tumor region in the CT (resp., PET) image.

To express our energy function, we start with the energy term E_{CT} for the segmentation of CT, which consists of two similar terms as in the well-known binary graph cut method [10]:

a region term and a boundary term. For each voxel $v \in \mathcal{I}$, a region cost $D_v(l_v)$ is assigned, which measures how well the voxel v with a label l_v fits into a given intensity model. Let \mathcal{N}_{CT} defines the neighboring relationship between voxels in \mathcal{I} . Then the boundary cost $V_{uv}(l_u, l_v)$ can be expressed as

$$V_{uv}(l_u, l_v) = \begin{cases} B_{uv} & \text{if } l_u \neq l_v \\ 0 & \text{if } l_u = l_v \end{cases} \quad (1)$$

where B_{uv} is the penalty of assigning different labels l_u and l_v to two neighboring voxels $(u, v) \in \mathcal{N}_{CT}$. Our energy term for CT segmentation takes the form:

$$E_{CT}(l) = \sum_{v \in \mathcal{I}} D_v(l_v) + \sum_{(u,v) \in \mathcal{N}_{CT}} V_{uv}(l_u, l_v), \quad (2)$$

The energy term E_{PET} for the segmentation of PET image has the same form as that used for CT. Let $D_{v'}(l_{v'})$ denote the region cost for voxel $v' \in \mathcal{I}'$, $V_{u'v'}(l_{u'}, l_{v'})$ denote the boundary cost between two neighboring voxels $(u', v') \in \mathcal{N}_{PET}$, where \mathcal{N}_{PET} defines the neighboring relationship between voxels in \mathcal{I}' . Then the energy term E_{PET} can be expressed as

$$E_{PET}(l) = \sum_{v' \in \mathcal{I}'} D_{v'}(l_{v'}) + \sum_{(u',v') \in \mathcal{N}_{PET}} V_{u'v'}(l_{u'}, l_{v'}). \quad (3)$$

As described above, the key to a successful segmentation is to make use of information from both PET and CT images. To incorporate context information between the modalities, a context term is added into the energy, which penalizes the segmentation difference between the two image datasets. Let (v, v') denote a pair of corresponding voxels in the CT image \mathcal{I} and the PET image \mathcal{I}' . The context cost $W_{vv'}(l_v, l_{v'})$ is defined, as follows.

$$W_{vv'}(l_v, l_{v'}) = \begin{cases} C_{vv'} & \text{if } l_v \neq l_{v'} \\ 0 & \text{if } l_v = l_{v'} \end{cases} \quad (4)$$

where $C_{vv'}$ is employed to penalize the disagreement between labels of corresponding voxels v and v' . Our context energy term takes the form:

$$E_{context}(l) = \sum_{(v,v')} W_{vv'}(l_v, l_{v'}). \quad (5)$$

The energy function of our co-segmentation is defined in the following way.

$$E(l) = E_{CT}(l) + E_{PET}(l) + E_{context}(l), \quad (6)$$

Our goal is to compute an optimal set l^* of labels such that the total energy is minimized. The label set l^* defines an optimal co-segmentation of PET-CT images.

Most previous co-segmentation algorithms in computer vision [49], [50], [51] work on a pair of images with similar (or nearly identical) foregrounds and unrelated backgrounds, and explicitly make use of histogram matching, which makes the models computationally intractable. Batra *et al.* recently applied the graph cut method for co-segmentation [52], in

which a common appearance model is assumed across all the segmented images. However, the PET and CT images may not have such a common appearance model. We propose a more flexible PET-CT context term $E_{context}$ to make use of the dual modality information.

B. Graph Construction

Our energy is minimized by solving a maximum flow problem in a corresponding graph, which admits a globally optimal solution in low-order polynomial time. In this section, we show how to encode our proposed energy terms through proper graph construction.

For energy terms E_{CT} and E_{PET} , a directed graph G is defined, which contains two node-disjoint subgraphs $G_{CT}(N, A)$ and $G_{PET}(N', A')$ for E_{CT} and E_{PET} (see Fig. 2), respectively. Note that two subgraphs use exactly the same structure to incorporate the region and boundary terms in the corresponding energy function. For the construction of $G_{CT}(N, A)$, every voxel $v \in \mathcal{I}$ has a corresponding node $n_v \in N$ in G_{CT} . Two dummy nodes, a source s and a sink t , are added into the graph. To encode the region term $\sum_{v \in \mathcal{I}} D_v(l_v)$, we put a t-link arc from source s to each node n_v with the weight $D_v(l_v = 0)$ and a t-link arc from each node n_v to the sink t with the weight $D_v(l_v = 1)$. The boundary term $\sum_{(u,v) \in \mathcal{N}_{CT}} V_{uv}(l_u, l_v)$ is enforced by adding n-links as follows. For each pair of neighboring voxels $(u, v) \in \mathcal{N}_{CT}$, two n-link arcs are introduced, one from n_u to n_v and the other in the opposite direction from n_v to n_u . The weight of each arc is set as B_{uv} . The subgraph $G_{PET}(N', A')$ can be built using the same way to encode the region term $\sum_{v' \in \mathcal{I}'} D_{v'}(l_{v'})$ and the boundary term $\sum_{(u',v') \in \mathcal{N}_{PET}} V_{u'v'}(l_{u'}, l_{v'})$ for the energy term E_{PET} . To solve them in a single maximum flow, two subgraphs share the same source s and sink t .

To enforce the context term $E_{context}(l)$, additional inter-graph arcs are added between G_{CT} and G_{PET} , named as “d-link” arcs. For every pair of corresponding voxels (v, v') , where v belongs to the CT image \mathcal{I} and v' is the corresponding voxel in the PET image \mathcal{I}' , two d-link arcs are added between corresponding nodes of two subgraphs, one from n_v to $n_{v'}$ and the other from $n_{v'}$ to n_v . The weight of arcs is set as $C_{vv'}$, which is the context cost penalizing the segmentation difference between two images (see the definition in Section III-A).

We thus finish the construction of the graph. Fig. 2 shows one example. Here the constructed graph G can be considered as a graph constructed for a 4-D image segmentation problem, where the 4-D image $\mathcal{I}_{4D} = \{ \mathcal{I}, \mathcal{I}' \}$ contains all voxels from the CT image \mathcal{I} and the PET image \mathcal{I}' . The neighboring setting between \mathcal{I} and \mathcal{I}' is defined by their correspondence relation. The regional cost for each voxel $v \in \mathcal{I}$ and $v' \in \mathcal{I}'$ is enforced by two t-link arcs, and the boundary costs between two neighboring voxels $(u, v) \in \mathcal{I}$ and $(u', v') \in \mathcal{I}'$ are enforced by the n-link arcs. Furthermore, the context term is encoded as the summation of the boundary costs enforced by the d-link arcs between corresponding voxel pairs (v, v') , where $v \in \mathcal{I}$ and $v' \in \mathcal{I}'$. Intuitively, these d-link arcs can be viewed as the n-link arcs between the two subgraphs associated with the two 3-D sub-images in the 4D image \mathcal{I}_{4D} . We thus transform the optimization problem as a 4-D segmentation problem, which is solvable by the minimum s - t cut method [10]. Specifically, a minimum s - t cut $\mathcal{C}^* = (A^*, \bar{A}^*)$ is found, which separates the graph G into two parts, the source set A^* and the sink set \bar{A}^* with $s \in A^*$ and $t \in \bar{A}^*$, and $A^* \cup \bar{A}^* = N \cup N' \cup \{s, t\}$. This minimum s - t cut, which can be obtained by solving a maximum flow problem in low-order polynomial time, defines an optimal segmentation minimizing the objective energy function Eq. (6). The target tumor volume on the CT image is defined by those voxels whose corresponding nodes in G_{CT} belong to the source set A^* . Similarly, the segmented tumor volume on the PET image is given by those voxels whose associated nodes in G_{PET} belong to the source set A^* .

IV. Lung Tumor Segmentation Methods

In this section, we apply the proposed graph model for a challenging task: lung tumor segmentation in PET-CT images. The tumor may invade into the adjacent area of the lung, including the chest wall, the mediastinal structure or the diaphragm, which increases the difficulty of tumor detection with anatomical imaging. The incorporation of PET information is necessary for a successful tumor delineation. Here our algorithm is applied for co-segmentation of PET-CT images, which can be divided into two steps. In the pre-processing step, the PET image is registered with the CT image. Then, our graph-based co-segmentation is conducted based on PET and CT images.

A. Registration

As a pre-processing, the PET image is registered with the CT image using rigid transformation based on the Elastix toolbox [53], which allows rotation and translation transformations. The PET image is upsampled using a cubic B-spline interpolator during registration to obtain a one-to-one voxel correspondence between the CT and the registered PET images. Note that the one-to-one correspondence may not be necessary. Our method can handle the case in which one PET voxel corresponds to a set of CT voxels.

We are aware that deformations due to breathing often require non-linear registration. However, affine registration is frequently used by physicians for PET-CT delineation of tumor volumes (e.g., Refs. [6], [54], [55]), for simplicity, we choose to use affine transformation in this study. In addition, our method allows differences between the tumor contours on PET and those on CT, which extensively alleviates the stringent requirement on registration. We will conduct experiments to demonstrate the feasibility of affine registration in this study.

B. Initialization

Initial seed points are required for our graph-based co-segmentation. In our application, one center point and two radii are given by the user for each target tumor based on the fused PET-CT image, from which two spheres are generated in an approximate tumor area. We require that the small one have to be completely inside the tumor and the large one have to be completely outside the tumor (see Fig. 3). In this way, all voxels inside the small sphere are taken as the seed set of the object for both CT and PET images, denoted by \mathcal{F} in the CT image \mathcal{I} and by \mathcal{F}' in the PET image \mathcal{I}' ; all voxels outside the large sphere are considered to be the seeds for the background, denoted by \mathcal{B} (resp., \mathcal{B}') in \mathcal{I} (resp., \mathcal{I}'). If there exists more than one tumor site in the dataset, then for each possible location, one center point as well as two radii are required as the initial input. Suppose we have M possible tumor locations in the image. Let \mathcal{F}_i (resp., \mathcal{F}'_i) and \mathcal{B}_i (resp., \mathcal{B}'_i) denote the seed sets associated with the location i in CT (resp., PET) for $i = 1, \dots, M$. Then the overall seed set of the object can be expressed as $\mathcal{F} = \mathcal{F}_1 \cup \mathcal{F}_2 \cup \dots \cup \mathcal{F}_M$ (resp., $\mathcal{F}' = \mathcal{F}'_1 \cup \mathcal{F}'_2 \cup \dots \cup \mathcal{F}'_M$). The overall seed set of the background has the form: $\mathcal{B} = \mathcal{B}_1 \cap \mathcal{B}_2 \cap \dots \cap \mathcal{B}_M$ (resp., $\mathcal{B}' = \mathcal{B}'_1 \cap \mathcal{B}'_2 \cap \dots \cap \mathcal{B}'_M$). Note that in this application, the CT and PET images share the same seed spheres.

C. Graph-based Co-segmentation

The graph is constructed following the method described in Section III-B. Two sub-graphs G_{CT} and G_{PET} are constructed for the segmentation of the CT and PET images, respectively. The cost functions are designed, as follows.

1) Cost functions for G_{CT} —For every voxel inside the small sphere ($v \in \mathcal{F}$), which is identified as a tumor seed by the user, its hard region costs are set as $D_v(l_v = 1) = 0$ and $D_v(l_v$

$= 0) = +\infty$. This makes sure that those voxels in \mathcal{F} will be labeled as the object. Similarly, for every voxel outside the large sphere ($v \in \mathcal{B}$), which is identified as the background seed, $D_v(l_v = 1) = +\infty$ and $D_v(l_v = 0) = 0$. Thus these voxels must be included in the background.

For any voxel lying between the two spheres ($v \in \mathcal{I} - \mathcal{F} - \mathcal{B}$), the region costs are designed based on how the intensity of voxel v fits into given intensity models. The image intensity of the tumor in CT roughly follows a gaussian distribution. Thus the region costs can be assigned according to the intensity distribution learned from the seed set of the object. Let i_v denote the intensity value for voxel v . The mean intensity value of all voxels in \mathcal{F} is denoted by \bar{i} and the corresponding standard deviation is σ . Then for any voxel $v \in \mathcal{I} - \mathcal{F} - \mathcal{B}$, the region term takes the form:

$$D_v(l_v=1) = -\lambda_1 \log Pr(i_v | l_v=1) \propto \frac{(i_v - \bar{i})^2}{\sigma^2} \quad (7)$$

$$D_v(l_v=0) = -\lambda_2 \log(1 - Pr(i_v | l_v=1)) \propto -\log(1 - \exp(-\frac{(i_v - \bar{i})^2}{\sigma^2})), \quad (8)$$

where λ_1 and λ_2 are two given scaling constants. Fig. 4(a) shows one typical slice of the cost image for the region term in CT.

For the cost design of the boundary term, a gradient-based cost is employed, which has a similar form as the well-known graph cut method in [10]. As described in Section III-A, B_{uv} denotes the penalty of assigning different labels to neighboring voxels $(u, v) \in \mathcal{N}_{cr}$. B_{uv} can be expressed as

$$B_{uv} = -\lambda_3 \log(1 - \exp(-\frac{|\nabla \mathcal{I}|^2(u, v)}{2\sigma_g^2})), \quad (9)$$

where $|\nabla \mathcal{I}|^2(u, v)$ denotes the squared gradient magnitude between u and v , σ_g is a given Gaussian parameter, and λ_3 is the scaling constant.

2) Cost functions for GpET—For every voxel $v' \in \mathcal{F}'$ or $v' \in \mathcal{B}'$, its hard region costs are set using the same form as we do for the CT image: $D_{v'}(l_{v'} = 1) = 0$ and $D_{v'}(l_{v'} = 0) = +\infty$ for $v' \in \mathcal{F}'$, and $D_{v'}(l_{v'} = 1) = +\infty$ and $D_{v'}(l_{v'} = 0) = 0$ for $v' \in \mathcal{B}'$. For all other voxels $v' \in \mathcal{I}' - \mathcal{F}' - \mathcal{B}'$ between two spheres, the region costs are computed based on the SUV values. As described in [56], the typical threshold value for tumor used in clinic application ranges from 15% to 50% of the maximum SUV in the image. Let $S(v')$ denote the SUV value for voxel v' . S_{max} denote the maximum SUV value in the image. Then for every voxel with a higher SUV value than 50% of S_{max} , it has a high likelihood to belong to a tumor. Similarly, for every voxel with a lower SUV value than 15% of S_{max} , it most likely belongs to the background. Based on this prior knowledge, our region cost functions take the form:

$$D_{v'}(l_{v'}=1) = \begin{cases} 0 & \text{if } S(v') > S_U \\ \lambda_4 C_{max} \cdot \left(1 - \frac{1}{1 + e^{-\frac{S(v') - S_L - \alpha}{S_U - S_L - \alpha}/\beta}}\right) & \text{if } S_L \leq S(v') \leq S_U \\ \lambda_4 C_{max} & \text{if } S(v') < S_L \end{cases} \quad (10)$$

$$D_{u'}(l_{u'}=0) = \lambda_4 C_{max} - D_{u'}(l_{u'}=1) \quad (11)$$

where C_{max} is the maximum region cost allowed; $S_U = 50\% \cdot S_{max}$ and $S_L = 15\% \cdot S_{max}$ are the upper and lower threshold values for the possible tumor region. A sigmoid function is employed to assign a high cost for a voxel with a low SUV value between S_L and S_U . Parameter a controls the curvature of the function and parameter β controls the center point of the function. λ_4 is a given coefficient. One typical slice of the cost image for the region term in PET is shown in Fig. 4(b).

The boundary term takes the same form as we have used in the CT images. The penalty $B_{u'v'}$ of assigning different labels to neighboring voxels $(u', v') \in N_{PET}$ can be expressed as

$$B_{u'v'} = -\lambda_5 \log(1 - \exp(-\frac{|\nabla \mathcal{I}'|^2(u', v')}{2\sigma_g'^2}))), \quad (12)$$

where $|\nabla \mathcal{I}'|^2(u', v')$ denotes the squared gradient magnitude between u' and v' . σ_g' and λ_5 are given parameters.

3) Cost functions for the context term—The context term in the energy function is designed to make use of the complementary information of PET and CT to improve the tumor boundary in the other modality. The segmentation difference between PET and CT should be penalized appropriately. To formulate the context cost functions, the region costs $D_v(l_v = 1)$ in the CT image and $D_{v'}(l_{v'} = 1)$ in the PET image are normalized between $[0, 1]$, denoted by N_v and $N_{v'}$, respectively. The normalization is to make sure that if two corresponding voxels have the same label (object or background), they will have similar region costs, that is, $D_v(l_v = 1) (D_v(l_v = 0))$ approximately equals to $D_{v'}(l_{v'} = 1) (D_{v'}(l_{v'} = 0))$. This allows us using different ways to design the region cost functions for CT and for PET. In our setting, a voxel with a higher region cost N_v or $N_{v'}$ is more likely to be the object, and a voxel with a lower cost is more likely to be in the background. Our context cost term $C_{vv'}$ ($l_v \neq l_{v'}$) can be described as follows:

$$C_{vv'} = \theta(1 - |N_v - N_{v'}|) + K, \quad (13)$$

where θ is a scaling constant, K is the minimum penalty for an inconsistent segmentation. Intuitively, if two corresponding voxels have the same label (object or background), they will have similar region costs and a larger context cost will be assigned to penalize the inconsistent segmentation between CT and PET. Note that the soft context cost term enables our method to follow the prominently salient features in each modality to obtain difference tumor volumes for PET and CT images.

V. Experimental Methods

Our method computes the tumor volume defined in CT as well as that defined in PET simultaneously. Two contours are generated, one on CT and one on PET. Ideally, we should validate both tumor volumes against manual delineation using the same set of PET-CT data. However, due to the clinical protocol in the application domain from which our PET-CT datasets were obtained, the manual contours are either available on CT or on PET, but not on both. We thus used two different sets of PET-CT data to validate the CT segmentation and PET segmentation, separately.

A. Lung cancer datasets for validation of CT segmentation

23 sets of 3-D FDG PET-CT images are obtained from different patients with lung tumors. Each set of images contains one CT image and one corresponding PET image acquired during the treatment planning of the radiotherapy. Images are acquired with a dual Positron Emission Tomography (PET) and Computed Tomography (CT) scanner developed by Siemens Medical Solutions USA, Molecular Imaging (Hoffman Estates, IL). The specific PET/CT scanner system used in this proposal is a Biograph 40. The PET system specifications include 6 mm spatial resolution (NEMA 2001), an 162 mm axial and 605 mm trans-axial field of view, 2 mm plane spacing, 500 psec coincidence time resolution, 4.4 cps/kBq, and $\leq 5\%$ variation in uniformity. Standard imaging protocols utilize 3 minutes per bed position and 90 minutes post-injection, reconstructed as $4 \times 4 \times 4 \text{ mm}^3$ voxels. CT scans are typically $1 \times 1 \times 2 \text{ mm}^3$ voxels acquired with 0.6 mm spatial resolution and 250 mAs, with and without contrast. The reconstructed matrix size for each CT slice is 512×512 , with a voxel size ranging from $0.98 \times 0.98 \times 2.00 \text{ mm}^3$ to $1.37 \times 1.37 \times 2.00 \text{ mm}^3$. For the PET images, the reconstructed matrix size ranges from 128×128 to 168×168 . The voxel size ranges from $3.39 \times 3.39 \times 2.02 \text{ mm}^3$ to $4.07 \times 4.07 \times 4.00 \text{ mm}^3$. As described in Section IV-A, the PET images were co-registered to the CT images in the pre-processing step and the experiments were conducted on the CT and the registered PET images, which have exactly the same size as the corresponding CT images.

The gross tumor volume (GTV) for each of the PET-CT datasets was traced by three independent experienced radiation oncologists on the CT images with the guidance of the corresponding PET images using the Pinnacle treatment planning system (Philips ADAC Pinnacle³). The PET image is either fused with the CT dataset or displayed side by side with CT for the delineation. The reference standard is generated by applying the Simultaneous Truth and Performance Level Estimation (STAPLE) algorithm [57] to the three manual delineations. Unfortunately, manual contours on PET alone for those lung cancer subjects were not available due to our current clinical practice standard. We thus did not validate the PET segmentation on these datasets.

The tumor size D was roughly quantified by the longest diameter of the manual segmentation in the axial image plane, as suggested in the Response Evaluation Criteria in Solid Tumors (RECIST) [58]. For our datasets, $15.78 \text{ mm} \leq D \leq 150.99 \text{ mm}$. The average tumor size is 81.65 mm^3 . The tumor sizes are estimated from the reference standard.

B. Head-and-neck cancer datasets for validation of PET segmentation

Two clinical PET-CT image pairs of different head-and-neck cancer patients, which contain 3 volumes of interests (VOI) in total, were used to validate the PET segmentation of our method. These datasets were used in the PET Contouring Grand Challenge in XII Turku PET Symposium (http://www.turkupetcentre.net/PET_symposium_XII_software_session/ContouringChallengeResults/index.php) for evaluating 33 PET-CT segmentation methods [59]. The images are obtained using the metabolic tracer ¹⁸F-Fluorodeoxyglucose (FDG) and a hybrid PET/CT scanner (GE Discovery). Three VOIs, including two tumor volumes and one lymph node volume, are manually delineated by 3 experts on 2 occasions with at least a week in between. A series of union masks are generated using the 6 manual delineations. The one with the closest absolute volume of the mean of all 6 expert manual delineations is used as reference standard. Detailed information about the data and how the reference standard is defined can be found in [59]. For these datasets, only manual contours on PET were available. So we only validate our method on PET segmentation with these datasets.

C. Parameter setting

In our CT contour validation experiments, the following parameter setting was empirically employed for all analyzed lung cancer datasets. For the segmentation of tumor in CT, boundary term provides a more important information compared with the region term. Thus we set coefficients as $\lambda_1 = \lambda_2 = 1$ for the regional term and $\lambda_3 = 5$, $\sigma_g = 0.5$ for the boundary term. For the segmentation in PET, regional information based on the SUV thresholding plays a key role. Thus we set coefficients as $\lambda_4 = 1$ for the regional term and $\lambda_5 = 0.1$, $\sigma'_g = 0.5$ for the boundary term. The scaling constant θ for the context term is set as 0.2. The minimum context penalty K is set as 0.1.

In our PET contour validation experiments on the head-and-neck cancer subjects, all parameters are kept the same as the CT contour validation on the lung cancer subjects, except that the upper SUV threshold for PET region cost $S'_{T_i} = 40\% \cdot S_{max}$ instead of $S_U = 50\% \cdot S_{max}$ in the lung cancer case.

D. Validation of CT segmentation on lung cancer subjects

The proposed algorithm was carried out on all 23 sets of PET-CT images for validation. For quantitative measurement, the segmentation performance on CT images was evaluated by comparing the computed results against the reference standard. Here we only use the segmentation results on CT for quantitative validation.

1) Evaluation measures—For volumetric error measurement, the Dice similarity coefficient (DSC) was computed, with

$$DSC = 2|V_m \cap V_c| / (|V_m| + |V_c|), \quad (14)$$

where V_m denotes the volume of the reference standard and V_c denotes the computed result. All DSC values were computed in 3-D. For the boundary surface distance error, the average symmetric surface distance (ASSD) with the form

$$ASSD = \frac{\sum_{a \in A} \min_{b \in B} d(a, b) + \sum_{b \in B} \min_{a \in A} d(a, b)}{N_A + N_B} \quad (15)$$

was used [60], where A denotes the boundary surface of the reference stand and B denotes the computed surface. a and b are mesh points on the reference surface and the computed surface, respectively. $d(a, b)$ represents the distance between a and b . N_A and N_B are the number of points on A and B , respectively.

2) Comparison with graph cut method solely using CT or PET—To determine the performance of our novel co-segmentation approach in comparison with the graph cut approach of solely using CT or PET, these three methods were applied to all 23 datasets with identical initialization and the same cost functions for the boundary term and the regional term in the corresponding image modalities. The computed scores of DSC and ASSD were computed for all three methods. Statistical significance of the observed differences was determined using Student t-tests for which p -value of 0.05 was considered significant.

3) Comparison with graph cut method using fused PET-CT images—As described in Section IV-C3, our method employs a soft context cost term, which allows

different segmented tumor volumes in PET and in CT. It is of interest to compare our co-segmentation method with the graph cut method on fused PET-CT images, which only produce an identical segmentation result on both modalities. The underlying assumption of the graph cut method on fused images is that the tumor volume defined in PET is the same as that defined in CT. However, the literature shows that PET and CT do not convey the same type of information, which is not necessarily complementary, but sometimes contradictory. Thus, the tumor volume defined in PET may not be identical to that defined in CT. In addition, the registration between PET and CT may not be perfect. The registration errors may also lead to tumor volume disagreement between PET and CT spatially.

For the fused PET-CT segmentation with graph cuts, each node in the graph is associated with a pair of corresponding voxels: one in PET and the other in CT. The region boundary costs are set as the sum of the original separate costs in PET and CT. To show the effectiveness of the proposed soft context costs, both methods were applied to all 23 datasets with identical initialization. The computed scores of DSC and ASSD were compared between the two methods.

4) Sensitivity to registration errors—Allowing different tumor contours defined on PET and on CT enables our method to be more tolerant to inaccurate registration. To demonstrate this, artificial registration errors were added to the transformation matrix computed with the Elastix toolbox. The resulting transformation matrix was used for registration between PET and CT. Then the proposed method was applied on the registered PET and CT images with the artificial transformation matrix. More specifically, we add 10% perturbation to the X, Y and Z components of the translation transformation between PET and CT. Separately, we add 10% perturbation to the three rotation angles between PET and CT to simulate errors in the rotation component of the transformation. The signs of the perturbation are randomly selected. The DSC and ASSD scores were computed and compared between before and after the artificial registration errors added.

5) Robustness to seed initialization—The observer who initialized the center point and two radii was asked to do the initialization again after over six months. The 2nd initialization was conducted without providing any information from the 1st initialization. The experiments on 23 lung cancer datasets were conducted again using the 2nd initialization. Accuracy scores including Dice Similarity Coefficient (DSC) and Average Symmetric Surface Distance (ASSD) were computed for the segmentation from the 2nd initialization.

E. Validation of PET segmentation on head-and-neck cancer subjects

Our method was used to segment the three VOIs of two head-and-neck PET-CT image datasets. For quantitative measurement, the segmentation performance on PET images was evaluated by computing the Dice similarity coefficient (DSC) scores against the reference standard. The DSC scores were compared with the 33 PET-CT segmentation methods [59] that were registered to the PET Contouring Grand Challenge. Our CT segmentation results were not used in this validation experiment.

VI. Results

A. Quantitative validation of CT segmentation

The computed Dice similarity coefficient (DSC) and average symmetric surface distance (ASSD) of segmented lung tumors are summarized in Table. I. Since the size of the target tumor has serious influence on the final quantitative value, e.g., the larger tumor tends to have a larger surface distance error, the results are presented as three groups according to the

tumor size. In both evaluation metrics, the proposed approach combining information from both PET and CT achieved a significant improvement in comparison with three other graph cut based methods: the graph cut method using only CT, the graph cut method using only PET, and the graph cut method using fused PET-CT images ($p < 0.05$).

Fig. 5 shows the performance comparison for all 23 lung datasets among the proposed algorithm and three other graph cut based methods ordered according to the tumor size. Generally speaking, our method not only shows an overall improvement of the segmentation, but also has a consistent segmentation performance for all tumors in the entire set of the 23 images. In contrary, the performance of the method using only CT or only PET is very uneven. For the CT-only method, the uneven performance is mainly caused by the leaking problem due to the less contrast of intensity between tumor and its surrounding tissues; while for the PET-only method, the blurring boundary is the major contribution to the uneven performance. Fig. 8(g)–(i) shows the segmentation performed on CT only, in which a serious leaking problem happens. In comparison with the method using fused PET-CT images, the proposed approach provides a more flexible control, which results in more accurate segmentation results.

Table II shows the Dice similarity coefficient (DSC) and average symmetric surface distance (ASSD) of segmented results with three different registrations: registration computed with the Elastix toolbox, registration added 10% artificial translation errors to the Elastix registration, registration added 10% artificial rotation errors to the Elastix registration. The scores demonstrate the robustness of our method to registration errors within a certain range.

As to the robustness of our method with respect to the seed initialization, Figure 6 shows the Dice similarity coefficient (DSC) and average symmetric surface distance (ASSD) of the segmented results with two different initializations. We can observe that our method achieved highly comparable results over those two initializations.

B. Quantitative validation of PET segmentation

Table III shows the DSC scores of our segmentation results on the three head-and-neck cancer VOIs, comparing against the top 7 methods in the PET Contouring Grand Challenge [59]. *Manual delineation methods* (MD) use a computer mouse to contour a VOI slice-by-slice. MD^b is performed by two independent, experienced physicians viewing only PET image data (MD_1^b and MD_2^b in Table III). MD^c performed on the PET images by a nuclear medicine physicist who used visual aids derived from the original PET. *Pipeline methods* (PL) are complex, multistep algorithms combining thresholding, region growing, watershed, morphological operations and other techniques. Method PL^b is a variant of the ‘Smart Opening’ algorithm, adapted for PET from the tool in [61]. Method PL^s is a new fuzzy segmentation technique for noisy and low resolution oncological PET images [37]. *Watershed methods* (WS) use variants of the classical algorithm in [62]. Method WS^b uses viscosity and markers to overcome the local minima problems in image gradient [63]. The thresholding methods were not among the top ranking ones. In fact, only one automated segmentation method outperformed the proposed method according to the DSC metric.

C. Illustrative results

Illustrative results of the experiments on the lung cancer subjects are shown in Fig. 8 for three views. From all views, our co-segmentation works quite well in both CT and PET images. Fig. 8 shows the segmentation results obtained using four compared methods. Our approach makes use of the advantages from both CT and PET images, exhibiting expected improvement in comparison with three other graph-cut methods.

Illustrative results of the experiments on the head-and-neck cancer subjects are shown in Fig. 9. Our approach achieved highly accurate PET segmentation results.

D. Execution time

Our algorithm was implemented in C++ on a Linux workstation (3GHz, 32GB memory). Current non-optimized implementation required about 6 minutes for each dataset. The execution time for the registration was about 60s.

Our graph-based co-segmentation took about 3 minutes.

VII. Discussion

Our proposed method makes use of advantages of both PET and CT to co-segment tumor from the dual modalities simultaneously. The novel feature lies on its global optimality for the PET-CT tumor segmentation with respect to the problem-specific objective function.

A. Importance of co-segmentation

Although PET-CT images have been routinely used in clinic qualitatively by physicians, many existing PET-CT segmentation algorithms only work for a single modality. The introduction of integrated PET-CT scanners has provided new opportunities to develop co-segmentation methods for tumor delineation by combining physiological information from PET with anatomical information from CT. Though utilizing both PET and CT information, the segmentation methods [29], [30], [31] are potentially more dependent on accurate registration than the proposed approach since they do not allow disagreement of tumor volumes on PET and on CT. First, image registration itself remains very challenging; even with the integrated PET-CT scanners, the acquired PET and CT images may not be well aligned due to the substantially longer acquisition time for PET. In addition, the tumor boundary defined in PET may not be identical to that defined in CT because of the different imaging mechanisms, even with perfect registration. Therefore, simultaneously segmenting tumor from both PET and CT while admitting the (subtle) difference of the boundaries defined in the two different modalities is more reasonable than those previous methods on fused PET-CT images, in which identical tumor boundaries are assumed. Our method is able to co-segment tumor using both PET and CT to accommodate the uncertainties in imaging and registration. Co-segmentation makes use of the high tumor contrast in PET and the exquisite anatomical structures provided by CT scans, enabling the identification and characterization of more lesions than either modality alone. A big challenge in PET segmentation is that pathological and physiological uptakes of the tracer cannot be distinguished; while the pathology and physiology changes are differentiable in CT. This further provides the rationale for the idea of co-segmentation.

B. Possible improvement

The initialization of the object and the background seed sets can potentially be automated or largely automated by using an approach similar to the one used in [64]. The approach proposed in [64] sets a threshold for the PET SUV value to define the object seeds first. Then starting from the object seeds, nearby voxels are searched to find voxels with SUV values lower than another threshold. Those voxels are defined as background seeds. These threshold parameters can be learned from training datasets, thus alleviating the human burden in specifying the object and background seed sets.

The context term in the energy function of our method is designed to make use of the complementary information of PET and CT to improve the tumor boundary in the opposite modality. Of course, the segmentation difference should be penalized appropriately. For

example, if the weights of inter-subgraph arcs are all set $+\infty$, then the tumor contours in PET and in CT are forced to be identical; while if those weights are all set 0, then it is equivalent to segmenting the two contours separately. Although in this study the parameters for those arc weight assignment were determined empirically, in the future we plan to apply machine-learning techniques to find appropriate parameter settings based on training datasets. In addition, a joint probabilistic models learned from both CT and PET for context cost design may also help. However, it may still pose a great challenge to determine appropriate parameters if the structural/anatomical and functional target volumes vary a lot. For the cases that PET and CT cannot provide enough complementary information to each other, our method may not be able to use the information of the other modality to improve the segmentation results.

Our method can be viewed as a general multi-modality co-segmentation framework. The low-level image features for a specific modality can be incorporated in the cost function design. The cost function design, in fact, is critically important for improving the performance of our method. In this study, we do not well utilize the PET uptake heterogeneity for the cost function design (i.e., $D_V(\cdot)$). In the future, we will investigate a better way to design the cost functions $D_V(\cdot)$ by making use of the SUV heterogeneity, and the new cost functions should be easy to be integrated in our framework.

In many cases, tumor grows adjacently to the boundary of its host. For instance, lung tumor may be in touch with lung parenchyma or close to the diaphragm; esophageal cancer attaches to the esophagus walls. The delineation of such a tumor from PET could be much more challenging due to the artifacts induced by the spill-over of signal from intensely avid lesions into adjacent normal structures. In that setting, however, the boundary surfaces of the tumor's adjacent structures can serve as valuable prior information to help separate the tumor from those structures. In the future, we plan to simultaneously segment those boundary surfaces from the CT scan as well as the tumor from both PET and CT datasets by integrating the graph searching method [44], [45], [65] with the graph cut method [10]. The integration of those two methods into one single optimization process, yet still admitting globally optimal solutions, will certainly become a more powerful tool for medical image analysis.

VIII. Conclusion

In this article, we propose a novel approach for the co-segmentation of the PET-CT images, which makes use of the strength from both modalities: the functionality information of PET and the anatomical structure information of CT. The target tumor volumes in PET and in CT are concurrently segmented with the help of the information acquired from the other modality. Our method was validated on a challenging task of segmenting lung tumor from 23 patient datasets and the challenging head-and-neck tumor from 2 patient subjects. The results clearly demonstrated the applicability and the improved performance of the proposed approach in comparison with the segmentation methods solely using PET or CT.

Acknowledgments

The contributions of T. Shepherd, who made the head-and-neck datasets and the manual tracings available to this study, are gratefully acknowledged. This work was supported in part by NSF grants CCF-0830402 and CCF-0844765; and NIH grants R01-EB004640 and K25-CA123112.

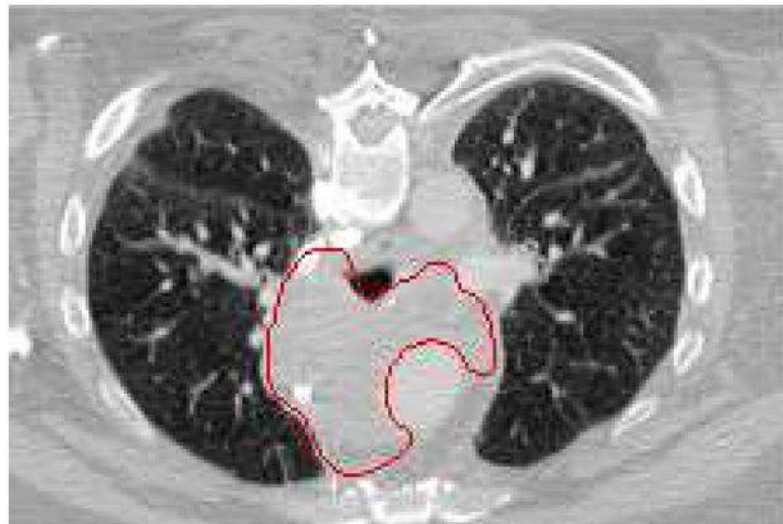
References

1. Riegel A, Berson A, Destian S, TNG, Tena L, Mitnick R, Wong P. Variability of gross tumor volume delineation in head-and-neck cancer using CT and PET/CT fusion. *International Journal of Radiation Oncology, Biology and Physics*. 2006; 65(3):726–732.
2. Bradley J, Thorstad W, Mutic S, Miller T, Dehdashti F, Siegel B, Bosch W, Bertrand R. Impact of FDG-PET on radiation therapy volume delineation in non-small-cell lung cancer. *International Journal of Radiation Oncology, Biology and Physics*. 2004; 59(1):78–86.
3. Baardwijk A, Bosmans G, Boersma L, Buijsen J, Wanders S, Hochstenbag M, Suylen R, Dekker A, Dehing-Oberije C, Houben R, Bentzen S, Kroonenburgh M, Lambin P, Ruyscher D. PET-CT-based auto-contouring in non-small-cell lung cancer correlates with pathology and reduces interobserver variability in the delineation of the primary tumor and involved nodal volumes. *International Journal of Radiation Oncology, Biology and Physics*. 2007; 68(3):771–778.
4. Ashamalla H, Rafla S, Parikh K, Mokhtar B, Goswami G, Kambam S, Abdel-Dayem H, Guirguis A, Ross P, Evola A. The contribution of integrated PET/CT to the evolving definition of treatment volumes in radiation treatment planning in lung cancer. *International Journal of Radiation Oncology, Biology and Physics*. 2005; 63(4):1016–1023.
5. Steenbakkers RJ, Duppen JC, Fitton I, Deurloo KE, Zipp LJ, Comans EF, Uitterhoeve AL, Rodrigus PT, Kramer GW, Bussink J, De Jaeger K, Belderbos JS, Nowak PJ, van Herk CR, Rasch M. Reduction of observer variation using matched CT-PET for lung cancer delineation: a three-dimensional analysis. *International Journal of Radiation Oncology, Biology, Physics*. Mar; 2006 64(2):435–48.
6. Fox JL, Rengan R, O'Meara W, Yorke E, Erdi Y, Nehmeh S, Leibel SA, Rosenzweig KE. Does registration of PET and planning CT images decrease interobserver and intraobserver variation in delineating tumor volumes for non-small-cell lung cancer? *International Journal of Radiation Oncology, Biology, Physics*. May; 2005 62(1):70–5.
7. Kiffer JD, Berlangieri SU, Scott AM, Quong G, Feigen M, Schumer W, Clarke CP, Knight SR, Daniel FJ. The contribution of 18F-fluoro-2-deoxyglucose positron emission tomographic imaging to radiotherapy planning in lung cancer. *Lung Cancer*. Mar; 1998 19(3):167–77. [PubMed: 9631364]
8. Munley MT, Marks LB, Scarfone C, Sibley GS, Patz EF, Turkington TG, Jaszczak RJ, Gilland DR, Anscher MS, Coleman RE. Multimodality nuclear medicine imaging in three-dimensional radiation treatment planning for lung cancer: challenges and prospects. *Lung cancer*. Feb; 1999 23(2):105–14. [PubMed: 10217614]
9. Nestle U, Walter K, Schmidt S, Licht N, Nieder C, Motaref B, Hellwig D, Niewald M, Ukema D, Kirsch CM, Sybrecht GW, Schnabel K. 18F-deoxyglucose positron emission tomography (FDG-PET) for the planning of radiotherapy in lung cancer: high impact in patients with atelectasis. *International Journal of Radiation Oncology, Biology, Physics*. Jun; 1999 44(3):593–7.
10. Boykov Y, Funka-Lea G. Graph cuts and efficient N-D image segmentation. *International Journal of Computer Vision*. 2006; 70(2):109–131.
11. Hong R, Halama J, Bova D, Sethi A, Emami B. Correlation of PET standard uptake value and CT window-level thresholds for target delineation in CT-based radiation treatment planning. *International Journal of Radiation Oncology, Biology, Physics*. 2007; 67:720–726.
12. Paulino AC, Koshy M, Howell R, Schuster D, Daivs LW. Comparison of CT- and FDG-PET-defined gross tumor volume in intensity-modulated radiotherapy for head-and-neck cancer. *International Journal of Radiation Oncology, Biology, Physics*. 2005; 61:1385–1392.
13. Scarfone C, Lavelly WC, Cmelak AJ, Delbeke D, Martin WH, Billheimer D, Hallahan DE. Prospective feasibility trial of radiotherapy target definition for head and neck cancer using 3-dimensional PET and CT imaging. *Journal of Nuclear Medicine*. 2004; 45(4):543–552. [PubMed: 15073248]
14. Bradley J, Thorstad WL, Mutic S, Miller TR, Dehdashti F, Siegel BA, Bosch W, Bertrand RJ. Impact of FDG-PET on radiation therapy volume delineation in non-small-cell lung cancer. *International Journal of Radiation Oncology, Biology, Physics*. 2004; 59:78–86.

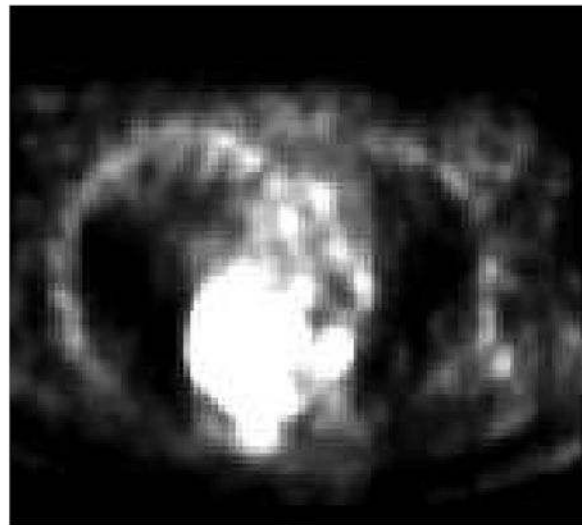
15. Erdi YE, Mawlawi O, Larson SM, Imbriaco M, Yeung H, Finn R, Humm JL. Segmentation of lung lesion volume by adaptive positron emission tomography image thresholding. *Cancer*. 1997; 80:2505–2509. [PubMed: 9406703]
16. Miller TR, Grigsby PW. Measurement of tumor volume by PET to evaluate prognosis in patients with advanced cervical cancer treated by radiation therapy. *International Journal of Radiation Oncology, Biology, Physics*. 2002; 53:353–359.
17. Ford EC, Kinahan PE, Hanlon L, Alessio A, Rajendran J, Schwartz DL, Phillips M. Tumor delineation using PET in head and neck cancers: threshold contouring and lesion volumes. *Medical Physics*. 2006; 33:4280–4288. [PubMed: 17153406]
18. Daisne JF, Sibomana M, Bol A, Doumont T, Lonneux M, Grgoire V. Tri-dimensional automatic segmentation of PET volumes based on measured source-to-background ratios: influence of reconstruction algorithms. *Radiotherapy and Oncology*. 2003; 69:247–250. [PubMed: 14644483]
19. Drever L, Robinson DM, McEwan A, Roa W. A local contrast based approach to threshold segmentation for pet target volume delineation. *Medical Physics*. 2006; 33:583–594.
20. Nestle U, Kremp S, Schaefer-Schuler A, Sebastian-Welsch C, Hellwig D, Rbe C, Kirsch CM. Comparison of different methods for delineation of 18F-FDG PET-positive tissue for target volume definition in radiotherapy of patients with non-small cell lung cancer. *Journal of Nuclear Medicine*. 2005; 46(8):1342–1348. [PubMed: 16085592]
21. Nehmeh SA, El-Zeftawy H, Greco C, Schwartz J, Erdi YE, Kirov A, Schmidlein CR, Gyau AB, Larson SM, Humm JL. An iterative technique to segment PET lesions using a Monte Carlo based mathematical model. *Medical Physics*. 2009; 36:4803–4809. [PubMed: 19928110]
22. Black QC, Grills IS, Kestin LL, Wong CO, Wong JW, Martinez AA, Yan D. Defining a radiotherapy target with positron emission tomography. *International Journal of Radiation Oncology, Biology, Physics*. 2004; 60:1272–1282.
23. Jentzen W, Freudenberg L, Eising EG, Heinze M, Brandau W, Bockisch A. Segmentation of PET volumes by iterative image thresholding. *Journal of Nuclear Medicine*. 2007; 48(1):108–114. [PubMed: 17204706]
24. Zaidi H, El Naqa I. PET-guided delineation of radiation therapy treatment volumes: a survey of image segmentation techniques. *European Journal of Nuclear Medicine and Molecular Imaging*. 2010; 37:2165–2187. [PubMed: 20336455]
25. Drever LA, Roa W, McEwan A, Robinson D. A comparison of three image segmentation techniques for target volume delineation in positron emission tomography. *Journal of Applied Clinical Medical Physics*. 2007; 8(2):93–109. [PubMed: 17592458]
26. Geets X, Lee J, Bol A, Lonneux M, Gregoire V. A gradient-based method for segmenting FDG-PET images: methodology and validation. *European Journal of Nuclear Medicine and Molecular Imaging*. 2007; 34:1427–1438. [PubMed: 17431616]
27. Hsu C, Liu C, Chen C. Automatic segmentation of liver PET images. *Computerized Medical Imaging and Graphics*. 2008; 32(7):601–610. [PubMed: 18722751]
28. Li H, Thorstad WL, Biehl KJ, Laforest R, Su Y, Shoghi KI, Donnelly ED, Low DA, Lu W. A novel PET tumor delineation method based on adaptive region-growing and dual-front active contours. *Medical Physics*. 2008; 35:3711–3721. [PubMed: 18777930]
29. El Naqa I, Yang D, Apte A, Khullar D, Mutic S, Zheng J, Bradley JD, Grigsby P, Deasy JO. Concurrent multimodality image segmentation by active contours for radiotherapy treatment planning. *Medical Physics*. 2007; 34(12):4738–4749. [PubMed: 18196801]
30. Yu H, Caldwell C, Mah K, Mozeg D. Coregistered FDG PET/CT-based textural characterization of head and neck cancer for radiation treatment planning. *IEEE Transactions on Medical Imaging*. 2009; 28:374–383.
31. Gribben, H.; Miller, P.; Hanna, GG.; Carson, KJ.; Hounsell, AR. MAP-MRF segmentation of lung tumours in PET-CT image. *IEEE International Symposium on Biomedical Imaging: From Nano to Macro*; 2009. p. 290-293.
32. Aristophanous M, Penney BC, Martel MK, Pelizzari CA. A gaussian mixture model for definition of lung tumor volumes in positron emission tomography. *Medical Physics*. 2007; 34:4223–4235. [PubMed: 18072487]

33. Hatt M, Lamare F, Bousson N, Roux C, Turzo A, Cheze-Lerest C, Jarritt P, Carson K, Salzenstein F, Collet C, Visvikis D. Fuzzy hidden Markov chains segmentation for volume determination and quantitation in PET. *Physics in Medicine and Biology*. 2007; 52:3467–3491. [PubMed: 17664555]
34. Potesil, V.; Huang, X.; Zhou, X. Automated tumor delineation using joint PET/CT information. *Proc. of SPIE Medical Imaging: Computer-aided Diagnosis*; 2007.
35. Hatt M, Cheze le Rest C, Turzo A, Roux C, Visvikis D. A fuzzy locally adaptive Bayesian segmentation approach for volume determination in PET. *IEEE Transactions Medical Imaging*. 2009; 28(6):881–893.
36. Boudraa AE, Champier J, Cinotti L, Bordet JC, Lavenne F, Mallet JJ. Delineation and quantitation of brain lesions by fuzzy clustering in positron emission tomography. *Computerized Medical Imaging and Graphics*. 1996; 20(1):31–41. [PubMed: 8891420]
37. Belhassen S, Zaidi H. A novel fuzzy C-means algorithm for unsupervised heterogeneous tumor quantification in PET. *Medical Physics*. 2010; 37:1309–1324. [PubMed: 20384268]
38. Hatt M, Cheze le Rest C, Descourt P, Dekker A, De Ruyscher D, Oellers M, Lambin P, Pradier O, Visvikis D. Accurate automatic delineation of heterogeneous functional volumes in positron emission tomography for oncology applications. *International Journal of Radiation Oncology, Biology, Physics*. 2010; 77:301–308.
39. Han, D.; Bayouth, JE.; Song, Q.; Taurani, A.; Sonka, M.; Buatti, JB.; Wu, X. Globally optimal tumor segmentation in PET-CT images: A graph-based co-segmentation method. *Proc. of the 22nd Int Conf on Information Processing in Medical Imaging (IPMI), Lecture Notes in Computer Science*; Kloster Irsee, Germany. July 2011; Springer; p. 245-256.
40. Wojak, J.; Angelini, ED.; Bloch, I. Joint variational segmentation of CT-PET data for tumoral lesions. 2010 IEEE International Symposium on Biomedical Imaging: From Nano to Macro; 2010. p. 217-220.
41. Felzenszwalb P, Huttenlocher D. Efficient graph-based image segmentation. *International Journal of Computer Vision*. 2004; 59(2):167–181.
42. Grady L. Minimal surfaces extend shortest path segmentation methods to 3D. *IEEE Transactions on Pattern Analysis and Machine Intelligence*. 2010; 32(2):321–334. [PubMed: 20075461]
43. Xu, L.; Stojkovic, B.; Zhu, Y.; Song, Q.; Wu, X.; Sonka, M.; Xu, J. Efficient algorithms for segmenting globally optimal and smooth multi-surfaces. *Proc. Biennial International Conference on Information Processing in Medical Imaging (IPMI)*; 2011.
44. Wu, X.; Chen, DZ. Optimal net surface problems with applications. *Proc. 29th International Colloquium on Automata, Languages and Programming*; 2002. p. 1029-1042.
45. Li K, Wu X, Chen DZ, Sonka M. Optimal surface segmentation in volumetric images - a graph-theoretic approach. *IEEE Transactions on Pattern Analysis and Machine Intelligence*. 2006; 28(1): 119–134. [PubMed: 16402624]
46. Yin Y, Zhang X, Williams R, Wu X, Anderson D, Sonka M. LOGISMOS - Layered Optimal Graph Image Segmentation of Multiple Objects and Surfaces: Cartilage segmentation in the knee joints. *IEEE Transactions Medical Imaging*. 2010; 29(12):2023–2037.
47. Song Q, Bai J, Garvin M, Sonka M, Buatti J, Wu X. Optimal multiple surface segmentation with shape and context priors. *IEEE Transactions on Medical Imaging*. 2013; 32(2):376–386. [PubMed: 23193309]
48. Delong, A.; Boykov, Y. Globally optimal segmentation of multi-region objects. *Proc. IEEE International Conference on Computer Vision*; 2009.
49. Mu, Y.; Zhou, B. Co-segmentation of image pairs with quadratic global constraint in MRFs. *Proc. of the 8th Asian Conf. on Computer Vision*; 2007. p. 837-846.
50. Mukherjee, L.; Singh, V.; Dyer, CR. Half-integrality based algorithms for cosegmentation of images. *Proc. of the IEEE Computer Society Conf. on Computer Vision and Pattern Recognition*; Miami, USA. 2009. p. 2028-2035.
51. Rother, C.; Minka, T.; Bae, A.; Kolmogorov, V. Cosegmentation of image pairs by histogram matching - incorporating a global constraint into MRFs. *Proc. of the IEEE Computer Society Conf. on Computer Vision and Pattern Recognition*; New York, USA. 2006. p. 993-1000.

52. Batra D, Kowdle A, Parikh D, Luo J, Chen T. Interactively co-segmenting topically related images with intelligent scribble guidance. *International Journal of Computer Vision (IJCV)*. 2011; 93(3):273–292.
53. Klein S, Staring M, Murphy K, Viergever M, Pluim J. Elastix: a toolbox for intensity-based medical image registration. *IEEE Transactions Medical Imaging*. 2010; 29:196–205.
54. Erdi YE, Rosenzweig K, Erdi AK, Macapinlac HA, Hu Y, Braban LE, Humm JL, Squire OD, Chui C, Larson SM, Yorke ED. Radiotherapy treatment planning for patients with non-small cell lung cancer using positron emission tomography (PET). *Radiotherapy and Oncology*. Jan; 2002 62(1): 51–60. [PubMed: 11830312]
55. Goerres GW, Kamel E, Heidelberg TNH, Schwitter MR, Burger C, von Schulthess GK. PET-CT image co-registration in the thorax: influence of respiration. *European Journal of Nuclear Medicine and Molecular Imaging*. Mar; 2002 29(3):351–360. [PubMed: 12002710]
56. Biehl KJ, Kong F, Dehdashti F, Jin J, Mutic S, Naqa IE, Siegel BA, Bradley JD. ¹⁸F-FDG PET definition of gross tumor volume for radiotherapy of non-small cell lung cancer: is a single standardized uptake value threshold approach appropriate? *Journal of Nuclear Medicine*. 2006; 47(11):1808–1812. [PubMed: 17079814]
57. Warfield SK, Zou KH, Wells WM. Simultaneous truth and performance level estimation (STAPLE): an algorithm for the validation of image segmentation. *IEEE Transactions on Medical Imaging*. Jul; 2004 23(7):903–21. [PubMed: 15250643]
58. Therasse P, Arbuck S, Eisenhauer E, Wanders J, Kaplan RS, Rubinstein L, Verweij J, Glabbeke MV, van Oosterom AT, Christian MC, Gwyther SG. New guidelines to evaluate the response to treatment in solid tumors. *Journal of the National Cancer Institute*. 2000; 92(3):205–216. [PubMed: 10655437]
59. Shepherd T, Teras M, Beichel R, Boellaard R, Bruynooghe M, Dicken V, Gooding M, Julyan P, Lee J, Lefevre S. Comparative study with new accuracy metrics for target volume contouring in PET image guided radiation therapy. *IEEE Transactions on Medical Imaging*. Jun; 2012 31(11): 2006–2024. [PubMed: 22692898]
60. van Ginneken, B.; Heimann, T.; Styner, M. 3D segmentation in the clinic: a grand challenge. *MICCAI Workshop on 3D Segmentation in the Clinic: A Grand Challenge*; 2007. p. 7-15.
61. Kuhnigk JM, Dicken V, Gornemann L, Bakai A, Wormanns D, Krass S, Peitgen HO. Morphological segmentation and partial volume analysis for volume try of solid pulmonary lesions in thoracic CT scans. *IEEE Transact*. 2006; 25:417–434.
62. Beucher, S.; Meyer, F. *Mathematical Morphology in Image Processing*. 1993. The morphological approach to segmentation: The watershed transformation; p. 433-482.
63. Lopez-Mir, F.; Naranjo, V.; Angulo, J.; Villanueva, E.; Alcaniz, MA.; Lopez-Celada, S. Aorta segmentation using the watershed algorithm for an augmented reality system in laparoscopic surgery. *Proc. of IEEE International Conference on Image Processing*; 2011. p. 2649-2652.
64. Bagci U, Udupa JK, Yao J, Mollura DJ. Co-segmentation of functional and anatomical images. *International Conference on Medical Image Computing and Computer-Assisted Intervention*. Jan; 2012 15(3):459–67.
65. Wu X, Chen DZ, Li K, Sonka M. The layered net surface problems in discrete geometry and medical image segmentation. *International Journal of Computational Geometry and Applications*. 2007; 17(3):261–296. [PubMed: 20221409]



(a)



(b)

Fig. 1. The PET-CT images. (a) One slice of a CT image for treatment planning of lung tumor (red line). (b) The corresponding PET image.

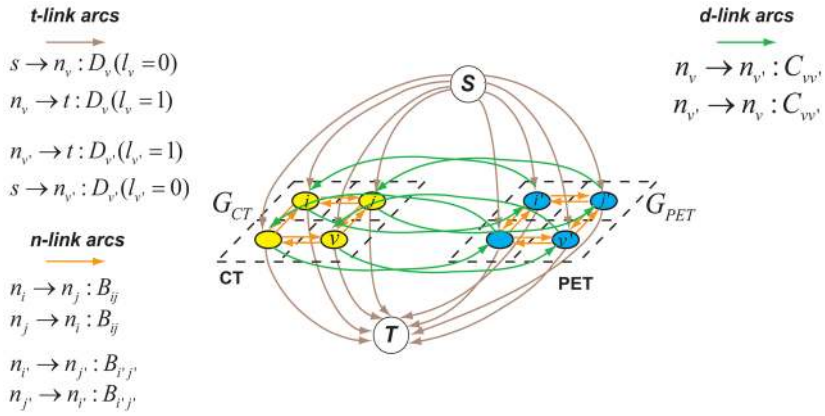


Fig. 2. Illustrating the graph construction of G with two sub-graphs G_{CT} and G_{PET} for the co-segmentation of PET-CT images. Three types of arcs are introduced. The t-link arcs (brown), n-link arcs (orange), and d-link arcs (green) encode the region costs, boundary costs, and the context penalties, respectively.

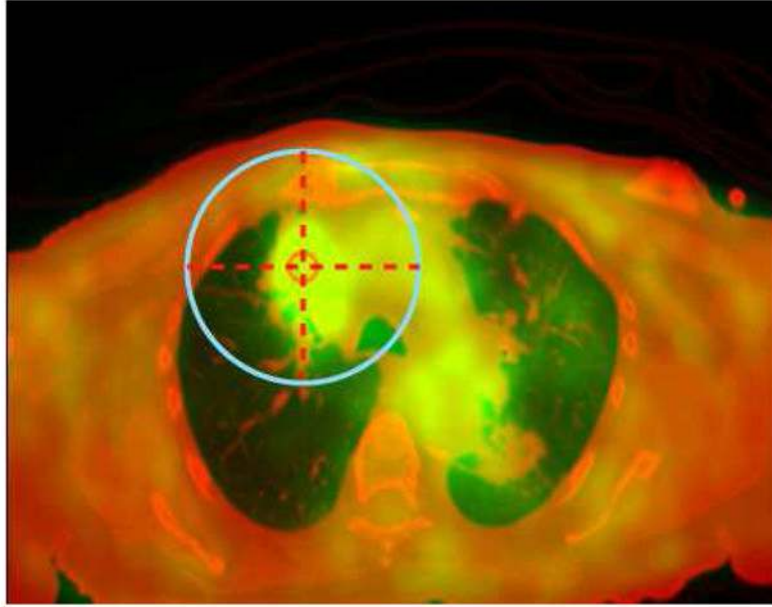
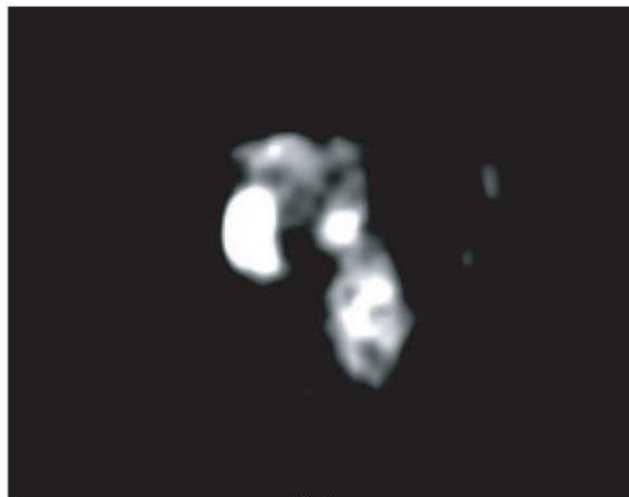


Fig. 3. Example slices of the initialization step in the fused image of CT (colored red) and PET (colored green). The orange sphere completely lies inside the tumor and the blue sphere completely contains the tumor. The center point is given by the cross point of two red lines.



(a)



(b)

Fig. 4. One typical slice of a cost image for the region term in (a) CT and (b) PET images. The target tumor boundary is labeled by the red contour. A larger intensity value indicates that the voxel is of the tumor in a higher probability.

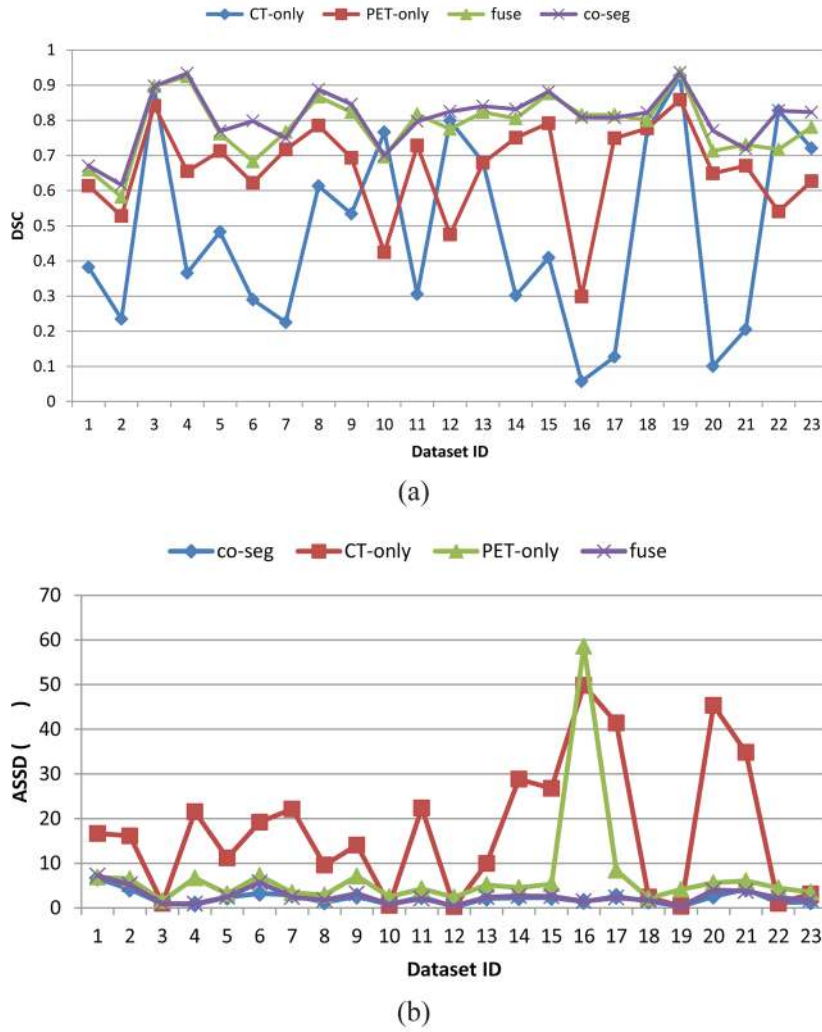
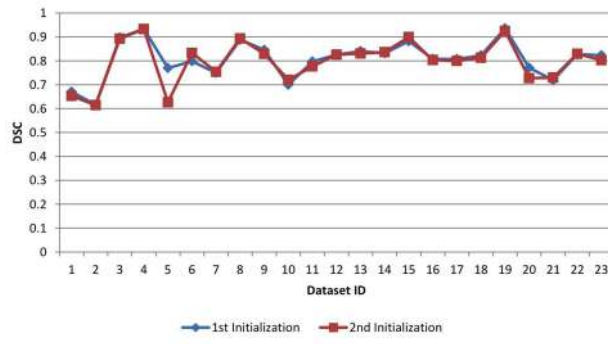
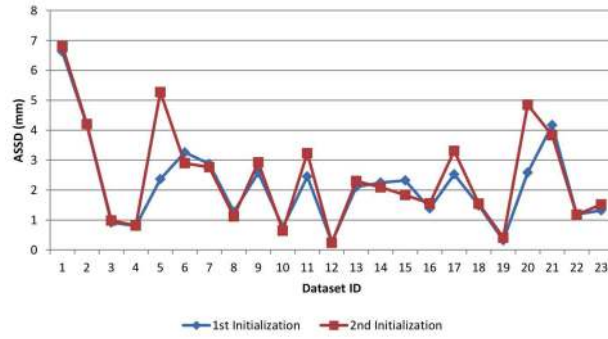


Fig. 5. Quantitative and comparative performance evaluation based on computed (a) DSC values and (b) ASSD values on 23 PET-CT lung cancer images, ordered according to the size of the tumor. Our method (blue) showed a relatively consistent results over all datasets compared to three other graph cut based methods: the graph cut method solely using CT (red), solely using PET (green), and the graph cut method using fused PET-CT images (orange).

NIH-PA Author Manuscript
NIH-PA Author Manuscript
NIH-PA Author Manuscript



(a) DSC's for different initializations



(b) ASD's for different initializations

Fig. 6. Quantitative results for the proposed method using different initializations.

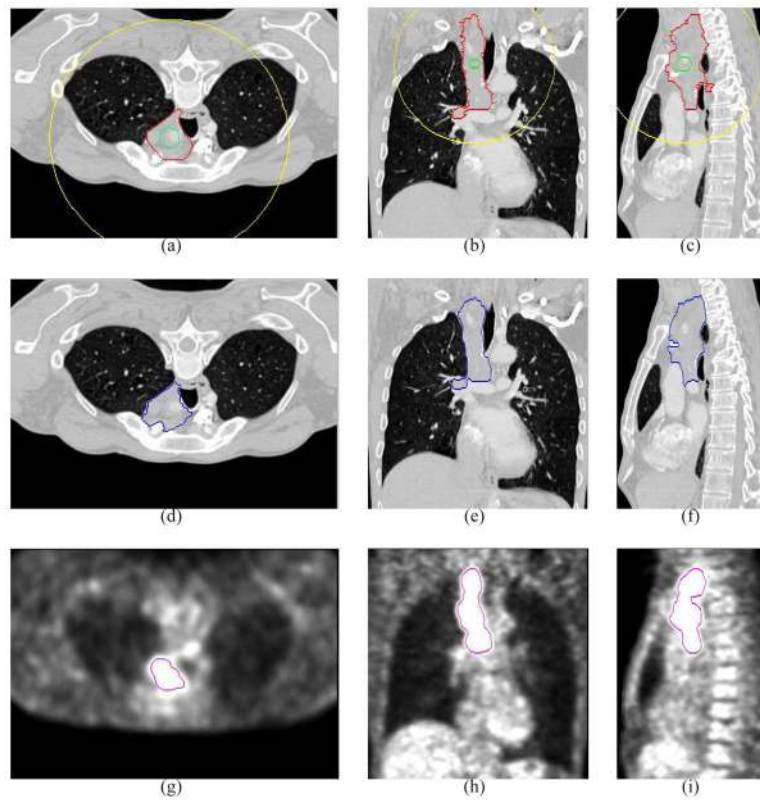


Fig. 7. Typical tumor segmentation in the transverse (left), coronal (middle) and sagittal (right) views. (a)–(c) 2-D slices of a 3-D CT image with the reference standard (red) and outlines of spherical initialization (green and yellow). (d)–(f) Proposed co-segmentation results in the CT image. (g)–(i) Co-segmentation results in the PET image.

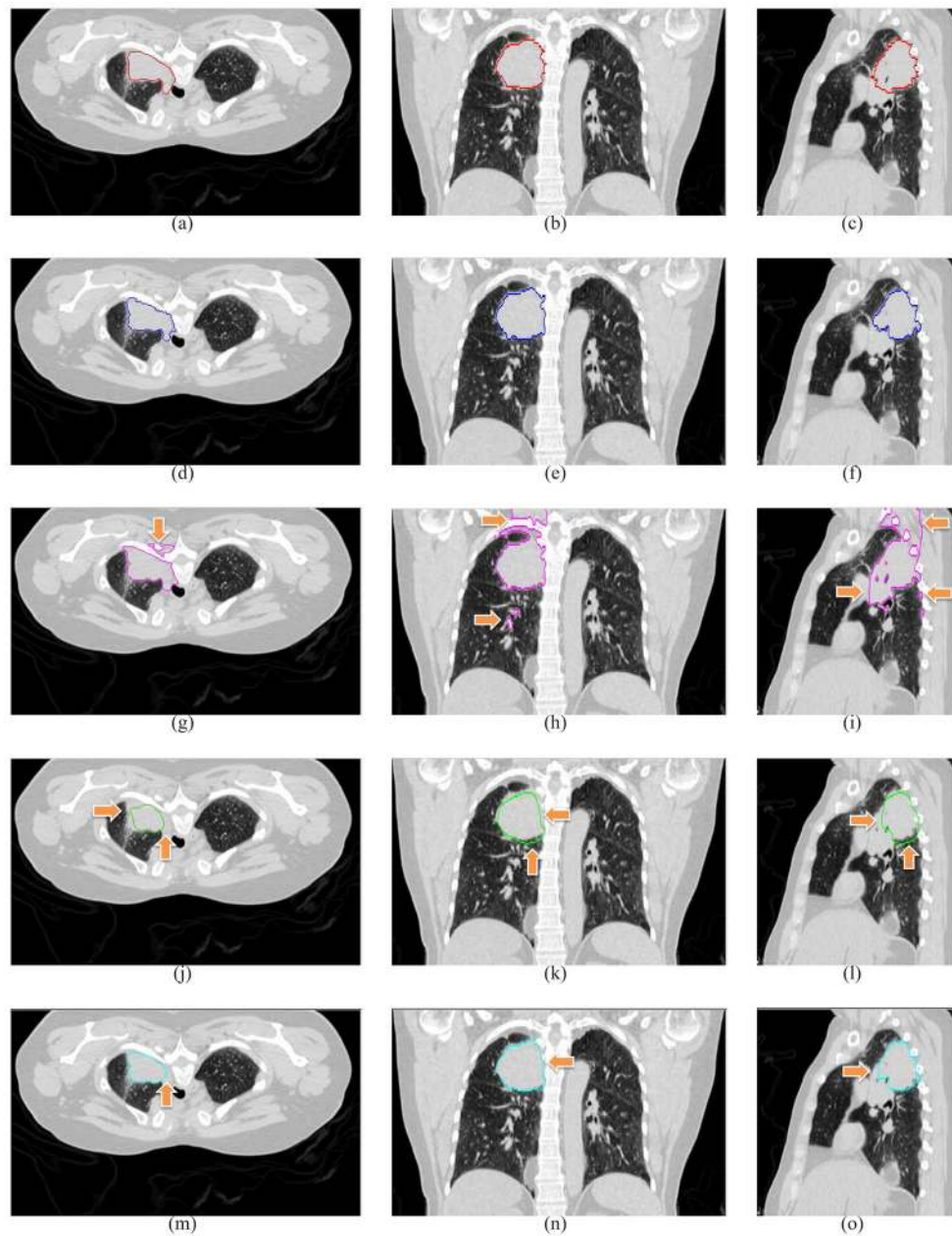


Fig. 8. Comparative segmentation results in the transverse (left), coronal (middle) and sagittal (right) views. (a)–(c) The manual segmentation results. (d)–(f) Our proposed co-segmentation results in the CT image. (g)–(i) The segmentation results by the graph cut method solely using the CT image. (j)–(l) The segmentation results by the graph cut method solely using the PET image. (m)–(o) The segmentation results by the graph cut method on the fused PET-CT image. The typical improvements of the proposed method in comparison with those three other methods are indicated by arrows.

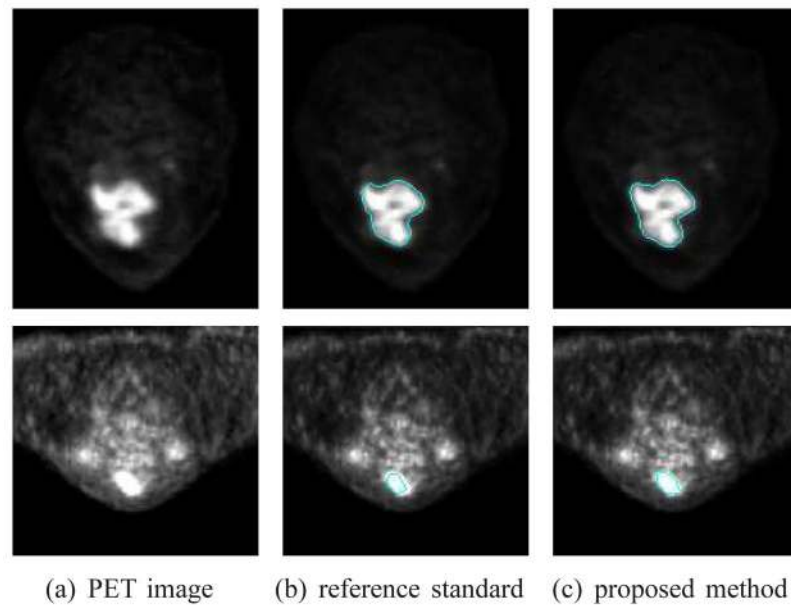


Fig. 9. Illustrative results of PET segmentation on head-and-neck cancer subjects.

Quantitative scores of segmented lung tumors using the proposed co-segmentation method in comparison with three other methods: the graph cut methods solely using CT, solely using PET and the graph cut method using fused PET-CT. The tumors are divided into three groups according to their sizes. All results are reported as mean \pm standard deviation.

TABLE I

Tumor size S (mm)	Num of datasets	DSC				ASSD (mm)			
		Proposed	CT Only	PET Only	fused PET-CT	Proposed	CT Only	PET Only	fused PET-CT
S < 50	5	0.82 \pm 0.07	0.81 \pm 0.07	0.59 \pm 0.15	0.78 \pm 0.08	0.77 \pm 0.43	1.05 \pm 1.07	3.40 \pm 0.84	1.12 \pm 0.77
50 \leq S < 100	11	0.82 \pm 0.08	0.42 \pm 0.25	0.68 \pm 0.14	0.81 \pm 0.08	2.06 \pm 0.95	19.83 \pm 14.58	9.56 \pm 15.66	2.28 \pm 1.15
S \geq 100	7	0.78 \pm 0.07	0.34 \pm 0.17	0.68 \pm 0.06	0.76 \pm 0.08	3.36 \pm 1.48	25.00 \pm 11.03	5.79 \pm 0.94	3.98 \pm 1.74
Overall	23	0.81 \pm 0.08	0.48 \pm 0.27	0.66 \pm 0.13	0.79 \pm 0.08	2.17 \pm 1.42	17.32 \pm 14.75	7.07 \pm 11.14	2.54 \pm 1.67

TABLE II

Quantitative performance scores of the proposed method with three different registrations between PET and CT. All results are reported as mean \pm standard deviation.

Metric	Elastix reg	10% translation err	10% rotation err
DSC	0.81 \pm 0.08	0.80 \pm 0.08	0.80 \pm 0.08
ASSD (mm)	2.17 \pm 1.42	2.39 \pm 1.70	2.32 \pm 1.42

TABLE III

Comparison of the proposed method against the top methods in the PET Contouring Grand Challenge [59] according to the DSC metric on the head-and-neck datasets

Rank	Methods	DSC
1	MD ^c	0.813 ± 0.093
2	MD ₂ ^b	0.805 ± 0.035
3	PL ^b	0.771 ± 0.105
4	our method	0.761 ± 0.106
5	PL ^g	0.749 ± 0.039
6	MD ₁ ^b	0.739 ± 0.040
7	PL ^c	0.723 ± 0.091
8	WS ^b	0.687 ± 0.108